Nanoscale Advances

ROYAL SOCIETY OF CHEMISTRY

PAPER

View Article Online
View Journal | View Issue

Cite this: *Nanoscale Adv.*, 2024, **6**, 1423

An "all-in-one" treatment and imaging nanoplatform for breast cancer with photothermal nanoparticles†

Yuping Fu,‡[a] Hongmei Zhang,‡[a] Jiahui Ye,‡[b] Changrong Chen,[d] Yaxuan Yang,[b] Baojuan Wu,[b] Xi Yin,[b] Jiajun Shi,[b] Yun Zhu,[e] Cheng Zhao *[c] and Weijie Zhang*[ab]

Drug delivery systems based on nanoparticles still face challenges of low efficacy and an inability to track treatment effects in tumor therapy due to biological barriers. This limitation hinders clinicians' ability to determine treatment effects and proper drug dosages, thus, ultimately impeding the further application and transformation of nanoplatforms. To address this challenge, an all-in-one nanoplatform for therapy and imaging is proposed. The nanoplatform is constructed by using nanoparticles through the co-encapsulation of the photothermal therapeutic agent IR780, the passively targeted drug OA@Fe_3O_4, and the chemotherapeutic drug paclitaxel. Under the guidance of magnetic navigation, the nanoparticles can enhance local enrichment of the drug, while the luminescence properties of IR780 enable drug tracking at the same time. Remarkably, the nanoparticles exhibit improved photothermal-chemotherapy synergy under magnetic targeting guidance, demonstrating antitumor effects in both *in vitro* and *in vivo* experiments. It is demonstrated that the use of these polymeric nanoparticles has significant potential for future biomedical applications and clinical decisions.

Received 24th September 2023
Accepted 22nd January 2024

DOI: 10.1039/d3na00814b

rsc.li/nanoscale-advances

Introduction

Breast cancer is the most prevalent cancer, accounting for 15% of all cancer types, with 280 000 new cases reported, surpassing even lung cancer.[1] Early and prompt treatment is crucial for improving patient prognosis and survival rates.[2–4] Treatment for breast cancer depends on the stage of cancer and often involves localized treatments such as surgery, radiation, and drug therapy to reduce and shrink tumors.[5,6] Intravenous chemotherapy drugs are frequently used due to their rapid onset of action. However, they lack specificity for tumor cells and can be easily metabolized by the liver and kidneys, leading to low bioavailability and increased side effects.[7–9] This can result in systemic side effects, including decreased immunity and a higher risk of infection, which can limit the use of medication and delay treatment, ultimately exacerbating the disease. Due to the constraints associated with monotherapy, there is a discernible trend toward adopting combination therapy in the current treatment paradigm. Pre-existing preclinical investigations have notably illustrated the favorable therapeutic outcomes achieved through the application of combined photothermal-chemotherapy. Moreover, the effectiveness of combination therapy integrating photothermal and chemotherapy, when guided by multimodal imaging, surpasses that of singular photothermal-chemotherapy approaches.[10,11] Furthermore, current treatments for breast cancer lack the ability to track and evaluate treatment efficacy, making it challenging for clinicians to adjust dosages and treatment regimens.[12] This limitation underscores the urgent need for more targeted and efficient drug delivery and evaluation systems for breast cancer treatment. To address these challenges, various techniques have been developed to improve targeted drug delivery and visualization therapy.[13–17] Among these methods, nanodelivery systems have emerged as promising tools for precise therapy and specific imaging, providing targeted delivery and tracking in a controllable manner.[18–25] In comparison to conventional drug treatment, nanoparticles have the ability to be retained in the tumor microenvironment, based on theit enhanced

[a]*Division of Breast Surgery, Department of General Surgery, Nanjing Drum Tower Hospital, Nanjing Drum Tower Hospital Clinical College of Traditional Chinese and Western Medicine, Nanjing University of Chinese Medicine, Nanjing, 210008, China. E-mail: dg1735099@smail.nju.edu.cn; zhangweijie1616@nju.edu.cn*

[b]*Division of Breast Surgery, Department of General Surgery, Nanjing Drum Tower Hospital, The Affiliated Hospital of Medical School, Nanjing University, Nanjing, 210008, China*

[c]*Department of Gastroenterology, Nanjing Drum Tower Hospital, The Affiliated Hospital of Medical School, Nanjing University, Nanjing, 210008, China*

[d]*Division of Emergency Surgery, Department of General Surgery, Nanjing Drum Tower Hospital, The Affiliated Hospital of Medical School, Nanjing University, Nanjing, 210008, China*

[e]*Division of Pharmacy Surgery, Department of General Surgery, Nanjing Drum Tower Hospital, The Affiliated Hospital of Medical School, Nanjing University, Nanjing, 210008, China*

† Electronic supplementary information (ESI) available. See DOI: https://doi.org/10.1039/d3na00814b

‡ Yuping Fu, Hongmei Zhang and Jiahui Ye contributed equally to this manuscript.

permeability and retention impact, and exhibit better tissue penetration.[26–28] Moreover, the large specific surface area of nanoparticles can enhance drug enrichment at the tumor site and improve therapeutic efficacy.[29,30] However, current efforts to improve nanoparticle enrichment *in vivo* remain limited. Additionally, it is challenging to detect the degree of nanoparticle enrichment at the tumor site, making it difficult to evaluate the therapeutic concentration and effect of

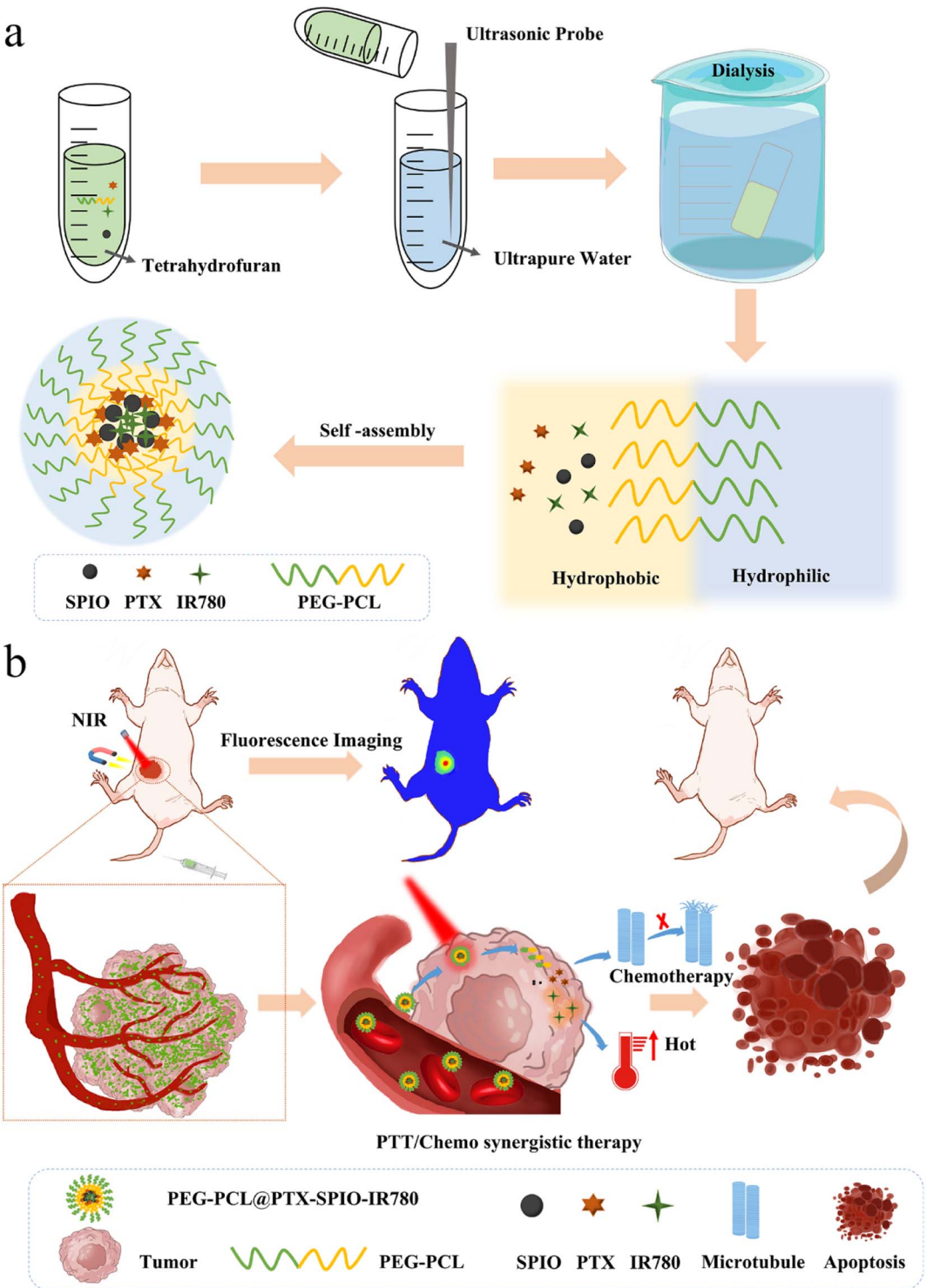

Fig. 1 Schematic illustration of the fabrication and application of the all-in-one nanoplatform. (a) Schematic illustration of the preparation of PEG-PCL@PTX-SPIO-IR780 nanoparticles. The system was constructed based on differences in the affinity of different materials for water. (b) An illustration of the process of PEG-PCL@PTX-SPIO-IR780 nanoparticles targeting breast cancer cells and exerting antitumor and tracking effects. Under the guidance of magnetic navigation, the nanoparticles could be enriched in the tumor, and provide imaging as well as therapeutic effects in a controllable manner.

nanoparticles. Therefore, there is an urgent need to develop novel systems that can make nanoplatforms more clinically relevant.

In order to meet the clinical needs of achieving the all-in-one goal of targeted therapy and tracking of drugs, we have developed novel photothermal polymeric nanoparticles, namely PEG-PCL@PTX-SPIO-IR780 (PPSI) nanoparticles, with magnetic guidance for tumor therapy, as depicted in Fig. 1. It was demonstrated that the nanoplatform could be established by exploiting the difference in the affinity of materials for water.[31] Briefly, the lipophilic segment polycaprolactone (PCL) of methoxy polyethylene glycol polycaprolactone (mPEG-PCL) encapsulated the drugs IR780, paclitaxel (PTX), and OA@Fe_3O_4 (SPIO), which were also lipid soluble, while the hydrophilic segment PEG was in direct contact with the water surface and formed nanoparticles by self-assembly. Under the guidance of magnetic navigation, the nanoparticles could be enriched in cell cytoplasm, which improved the drug uptake in cells. Furthermore, the developed nanoparticles could target the tumor site with magnetic navigation in a breast tumor mice model. The excellent tissue penetration enabled this system to exhibit good capabilities in *in vivo* imaging and photothermal therapy in the presence of IR780, which could show the tumor morphology and drug dose in a visible form. We have also demonstrated that *in vivo*, the synthetic effect of photothermal therapy and chemotherapy could induce cell death and reduce the tumor size, thus improving the overall treatment outcome. These indicated that this all-in-one nanoplatform is valuable for biomedical applications and clinical decisions.

Methods

Materials and animals

PEG-PCL was purchased from Daigang Company (Shandong, China). SPIO (OA@Fe_3O_4) was purchased from Nanjing Nanoeast Biotech Co. Ltd. Paclitaxel (PTX) and IR780 were bought from Macklin (Shanghai, China). THF was purchased from Sinopharm Chemical Reagent Co. Ltd (Beijing, China). Calcein-AM/PI was purchased from Nanjing Kaiji Biological Co. Ltd. PBS, fetal bovine serum (FBS) and Dulbecco's modified eagle medium (DMEM) were purchased from SenBeiJia Biological Technology Co. Ltd (Nanjing, China). All female BALB/c mice (4–5 weeks) were purchased from the Shanghai Research Institute of Family Planning. All cells were cultured in DMEM containing 10% FBS at 37 °C and 5% CO_2. All animals were handled in strict accordance with the standards in the Guide for the Care and Use of Laboratory Animals, and their use was in accordance with the terms of the Code of Practice for the Care and Use of Animals of Nanjing Hospital Affiliated to Nanjing Medical University. The Animal Ethics Committee of Nanjing Hospital affiliated to Nanjing Medical University approved all animal experimental protocols.

Preparation of PEG-PCL@PTX-SPIO-IR780 nanoparticles

IR780 (1.0 mg), SPIO (200 μL, 1 mg mL^{-1}), PTX (1.0 mg) and PEG-PCL were solubilized in THF, and then added to ultrapure water for sonication. The resulting solution was transferred to a dialysis bag and then centrifuged for 10 min and finally filtered through a 0.45 μm membrane to obtain the final drug-loaded nanoparticles. IR780 iodide and PTX loading content were calculated from UV-vis absorption spectra.

Characterization

The size and surface zeta potential of the prepared nanoparticles were calculated by using a Brookhaven BI-90Plus laser particle size analyzer. The morphological characterization of the prepared nanoparticles was visualized by TEM. The UV-vis absorption spectra were collected by using an ultra-micro spectrophotometer.

In vitro magnetic response characterization

A magnet was attached to the side of a transparent container, which was filled with PPSI nanoparticles and PEG-PCL@PTX-IR780 nanoparticle solution, to detect the magnetic properties of the nanoparticles. Agarose was used to simulate tissues to assess the magnetic responsiveness of nanoparticles in human tissues.

In vitro photothermal effect

Equivalent volumes of water, PEG-PCL nanoparticles, PEG-PCL@PTX-SPIO nanoparticles, and PPSI nanoparticles (60 μg mL^{-1}, IR780) were placed in Eppendorf tubes, and were irradiated by using an 808 nm laser at 2 W cm^{-2} for 6 min. The temperature variation was detected and recorded by using an infrared thermal imager at 30 s intervals. The PPSI nanoparticles were placed in an Eppendorf tube and irradiated for 6 min, and the temperature and cooling time were recorded.

Drug release

The drug release was characterized under three sets of experimental conditions (PPSI; pH 5.5, pH 5.5 + L, pH 7.4). Briefly, the nanoparticles (2 mL) were added to separate dialysis bags. Then, the bags were transferred into centrifugal tubes comprising 28 mL of PBS buffer, and then the tubes were shaken at 200 rpm at 37 °C. After shaking for 1 h, the pH 5.5 + L group was subjected to an 808 nm NIR laser (2 W cm^{-2}, 10 min) treatment, and then the shaking was continued. At regular intervals (0, 1, 3, 5, 7, 9, 12, 24, 48 and 72 h), a certain amount of dialysate was collected from each experimental group, and the container was filled with an equivalent volume of buffer.

In vitro cytotoxicity

The biocompatibility of PEG-PCL and PEG-PCL@SPIO nanoparticles and the cytotoxicity of nanoparticles *in vitro* were assessed by using cell counting kit (CCK-8) assays. 3T3 and 4T1 cells were seeded on a 96-well plate to grow. Then 3T3 cells were incubated with PEG-PCL and PEG-PCL@SPIO nanoparticles, and 4T1 cells were incubated with free PTX, free IR780, and PPS, PSI or PPSI nanoparticles, respectively, at different concentrations. The PBS group was set as a control. For PPSI + M and PPSI + L + M groups, magnets were placed in the bottom of the 96-

well plate immediately after drug addition to provide external magnetic force. Moreover, cells in PBS + L, IR780 + L, PSI + L, PPSI + L and PPSI + L + M groups were subjected to 808 nm laser illumination (2 W cm^{-2}, 10 min) after drug incubation for 24 h. And then, the CCK-8 assay reagent was added after 24 hours of cell incubation. After further incubation for a certain time, the absorbance at 450 nm was analyzed by enzyme markers to determine the cell viability. A fluorescence microscope was utilized to evaluate the apoptosis of cells. The tumor cells were cultured on a 24-well plate. After incubation of the cells for 24 h, the cells were continually incubated with different formulations. The IR780 + L, PSI + L, PPSI + L and PPSI + L + M groups were irradiated with 808 nm NIR light. Finally, the cells were stained and the cell killing efficiency was observed under a fluorescence microscope.

Cellular uptake

Confocal laser scanning microscopy (CLSM) was applied to evaluate the cellular uptake potential of PPSI nanoparticles. The 4T1 cells were cultured on a confocal imaging dish and co-cultured with PPSI nanoparticles or free IR780 for 4 h. The PPSI group had magnets attached to the bottom of the confocal dish (20 μg mL^{-1}, IR780). Finally, the treated cells were stained to assess the cellular uptake of nanoparticles.

Mouse tumor model

BALB/c mice (female; 20 g) were purchased from the Shanghai Research Institute of Family Planning. By *in situ* injection, 1×10^6 4T1 cells were implanted into the mammary fat pad of mice. When the tumor size reached the desired volume, further experiments were performed.

In vivo biodistribution

The distribution study was performed on an *in vivo* imaging system (IVIS). Successfully molded mice were randomly assigned to three groups (free IR780; PPSI; PPSI + M, $n = 3$) and injected with IR780 (2 mg kg^{-1}) through the caudal vein. At 1, 6, 12, 24, and 48 h post-injection, the mice were anaesthetized by being placed onto an atmosphere system, and then an IVIS was used for imaging. The mice were euthanized after 48 h, and the major organs, including the heart, liver, spleen, lung, kidney and tumor were sorted out for imaging.

In vivo synergistic therapeutic effect

When the tumors reached about ~100 mm^3 in size, successfully molded mice were randomly assigned to five groups and intravenously injected with saline ($n = 4$), saline + L ($n = 4$), IR780 (0.4 mg kg^{-1} IR780, $n = 4$) and PPSI (0.4 mg kg^{-1} IR780, $n = 4$) on days 0, 2, and 4 (once per day). Successfully molded mice also were randomly assigned to six groups and intravenously injected with saline ($n = 4$), PTX (2 mg kg^{-1}, $n = 4$), and PPSI (2 mg kg^{-1} PTX, $n = 4$) on days 0, 2, and 4 (once per day). The mice in saline + L, IR780 + L, PPSI + L and PPSI + L + M groups were subjected to laser illumination (2 W cm^{-2}, 10 min) after 24 h of drug injection. The tumors in the PPSI + M group and PPSI + L + M group were attached with magnets after injection. The tumor dimension was measured every two days. The mouse body weight was also tracked. The mice were all euthanized on day 16, and the tumors as well as major organs were sorted and stained with HE, TUNEL and IHC to estimate the effectiveness of tumor suppression and therapeutic safety. Blood was taken from the mice for routine and biochemical tests.

Statistical analysis

The one-way analysis of variance (ANOVA) test was carried out to analyze all experimental data. $P^* < 0.05$ and $P^{**} < 0.001$ was considered statistically significant, and remarkably statistically significant, respectively.

Results and discussion

Fabrication and characterization of PEG-PCL@PTX-SPIO-IR780 nanoparticles

In a typical experiment, PPSI nanoparticles were fabricated using a versatile and straightforward dialysis method. To be specific, hydrophobic SPIO particles coated with oleic acid, IR780, the lipophilic drug PTX and polymer PEG-PCL dissolved in tetrahydrofuran (THF), were added to ultrapure water. The resulting mixture was then subjected to dialysis for 24 hours to obtain nanoparticles. Exploiting the amphiphilicity of the binary copolymer PEG-PCL, the hydrophobic chain segments of PCL in the copolymer were repelled by water molecules to form spherical nanostructures, and in the process, drugs that are likewise hydrophobic were incorporated into the aggregates. The PPSI nanoparticles and PEG-PCL nanoparticles had average sizes of 158.15 nm and 135.76 nm, and a zeta potential of about 14.66 mV and −12.97 mV, respectively, suggesting a uniform size distribution (Fig. 2a–c, Table S1†). The increasing size demonstrated the successful encapsulation of drugs. The size of the prepared nanoparticles was below 200 nm, indicating their ability to penetrate through the interstitial space of tumor blood vessels. Additionally, the nanoparticles exhibited a generally spherical shape under a transmission electron microscope (TEM) with PDI values of about 0.267 (Fig. 2d, Table S1†). In transmission electron microscopy (TEM), the sample preparation involved dehydration and drying steps, at which time the nanoparticles shrunk, whereas when performing the DLS assay, the nanoparticles exhibited swelling behavior, and thus the nanoparticle size shown in the TEM image was smaller than those in the DLS assay.[32] Also, the UV-vis absorption spectra confirmed the successful incorporation of PTX and IR780 into nanoparticles (Fig. 2e). The full wavelength absorption spectra of PPSI nanoparticles revealed two absorption peaks at 229 nm and 780 nm, which were ascribed to PTX and IR780. The drug loading capacities (LC%) of PTX, IR780 and SPIO in PPSI nanoparticles were 4.07%, 0.82% and 0.36%. And the encapsulation efficiency (EE%) of PTX, IR780 and SPIO in PPSI nanoparticles was 81.38%, 16.39% and 35.99% (Table S2†). Moreover, the size of the prepared nanoparticles showed a little fluctuation for approximately two weeks when stored at 4 °C,

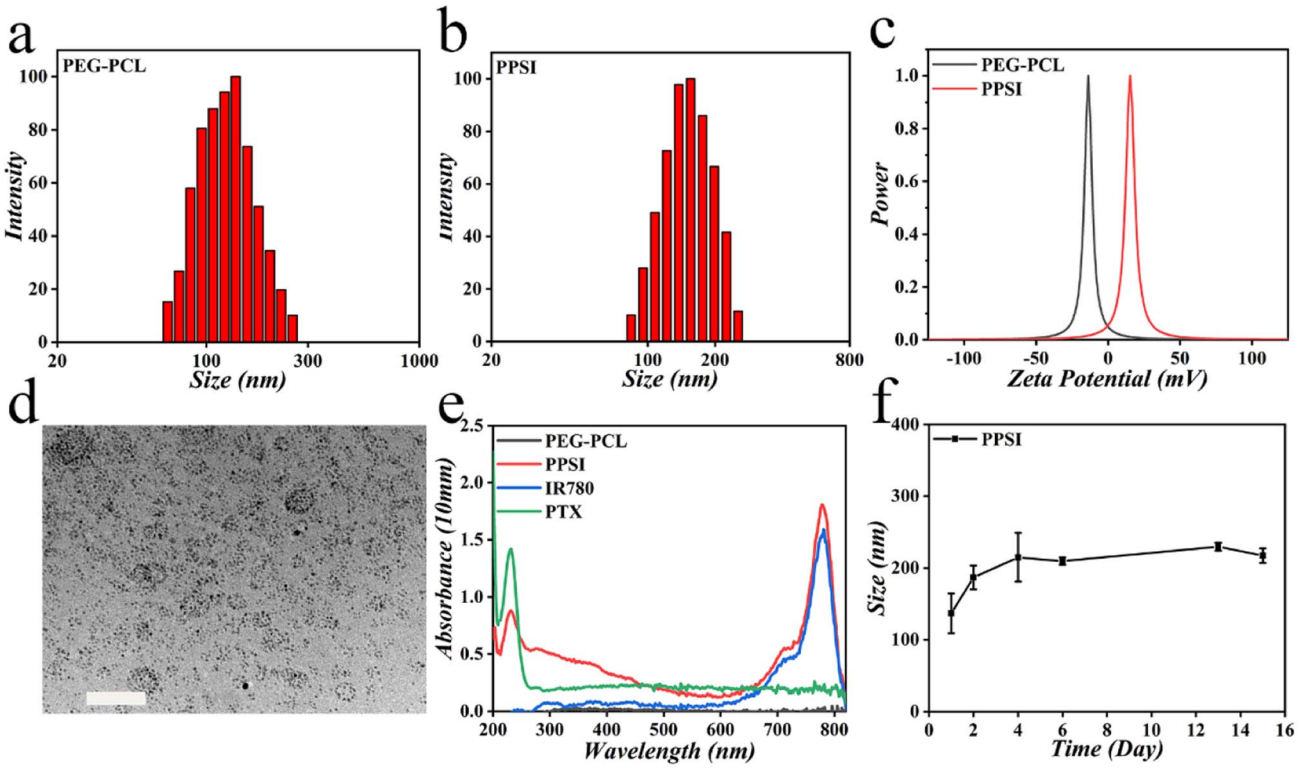

Fig. 2 Characterization of PPSI nanoparticles. (a) and (b) The size distribution of PPSI nanoparticles and PEG-PCL nanoparticles obtained by dynamic light scattering (DLS). (c) Zeta potentials of PPSI nanoparticles and PEG-PCL nanoparticles. (d) TEM image of PPSI nanoparticles. Scale bar: 200 nm. (e) UV-vis absorption spectra of the PEG-PCL nanoparticles, PPSI nanoparticles, and free IR780 and PTX solution. (f) The sizes of PPSI nanoparticles at 4 °C.

but the size was still relatively stable, indicating their stability for practical application (Fig. 2f). As a result, a novel particle with magnetic control and imaging properties was prepared for targeted and synergistic tumor therapy.

In vitro photothermal effect and magnetic response

To investigate the manual controllability of nanoparticles, the nanoparticles were placed in cuvettes and agarose, which simulated tissues. Notably, the PPSI group displayed excellent magnetic responsiveness compared to the PEG-PCL@PTX-IR780 group, as evident from their gradual magnetic attraction towards one side of the cuvette over time (Fig. 3a). To simulate the behavior of nanoparticles *in vivo*, agarose was used to mimic the tissue environment, where the fluid in the container was observed to reduce over time due to the osmotic effect. Concurrently, the nanoparticles were attracted to one side by the magnetic field, and more nanoparticles were attracted to the agarose, verifying the penetration of nanoparticles into the tissue. Magnets with different contact areas had different abilities to attract, ultimately causing the group with the larger contact area to attract more nanoparticles at the same time (Fig. 3bi and ii). These results clarified the superior magnetic responsiveness of PPSI nanoparticles, laying the groundwork for further investigations.

Additionally, when exposed to 808 nm laser irradiation, the temperature of the PPSI group, in the presence of IR780, exhibited a significant increase (up to 62.2 °C). Conversely, the temperature of groups without IR780 (water, PEG-PCL, and PEG-PCL@PTX-SPIO) showed only a slight temperature increase (up to 27.6 °C, 26.8 °C and 27.5 °C, respectively). These observations confirmed the pronounced photothermal effect of PPSI nanoparticles and further demonstrated the successful encapsulation of IR780 and its stability and functionality in the system (Fig. 3c and d). We investigated the photothermal transfer efficiency of PPSI nanoparticles. The results show that the photothermal conversion efficiency of the PPSI nanoparticles is 25.43% (Fig. S1†), which is higher than that of free IR780 (17%).[33] Overall, these results suggested that PPSI nanoparticles possessing photothermal conversion capabilities had the potential to enhance local drug accumulation and improve drug utilization at the tumor site, thus enhancing the overall anti-tumor efficacy.

Cellular uptake

To understand the penetration and accumulation of PPSI under practical conditions, the nanoparticles were cultured with cells for further analysis. Cellular uptake studies were performed in 4T1 cells using IR780's own fluorescence imaging characteristics, and the phagocytosis of PPSI nanoparticles was directly observed with a confocal laser scanning microscope (CLSM). The highest vigorous red fluorescence intensity was observed by CLSM in the PPSI nanoparticles with the external magnetic

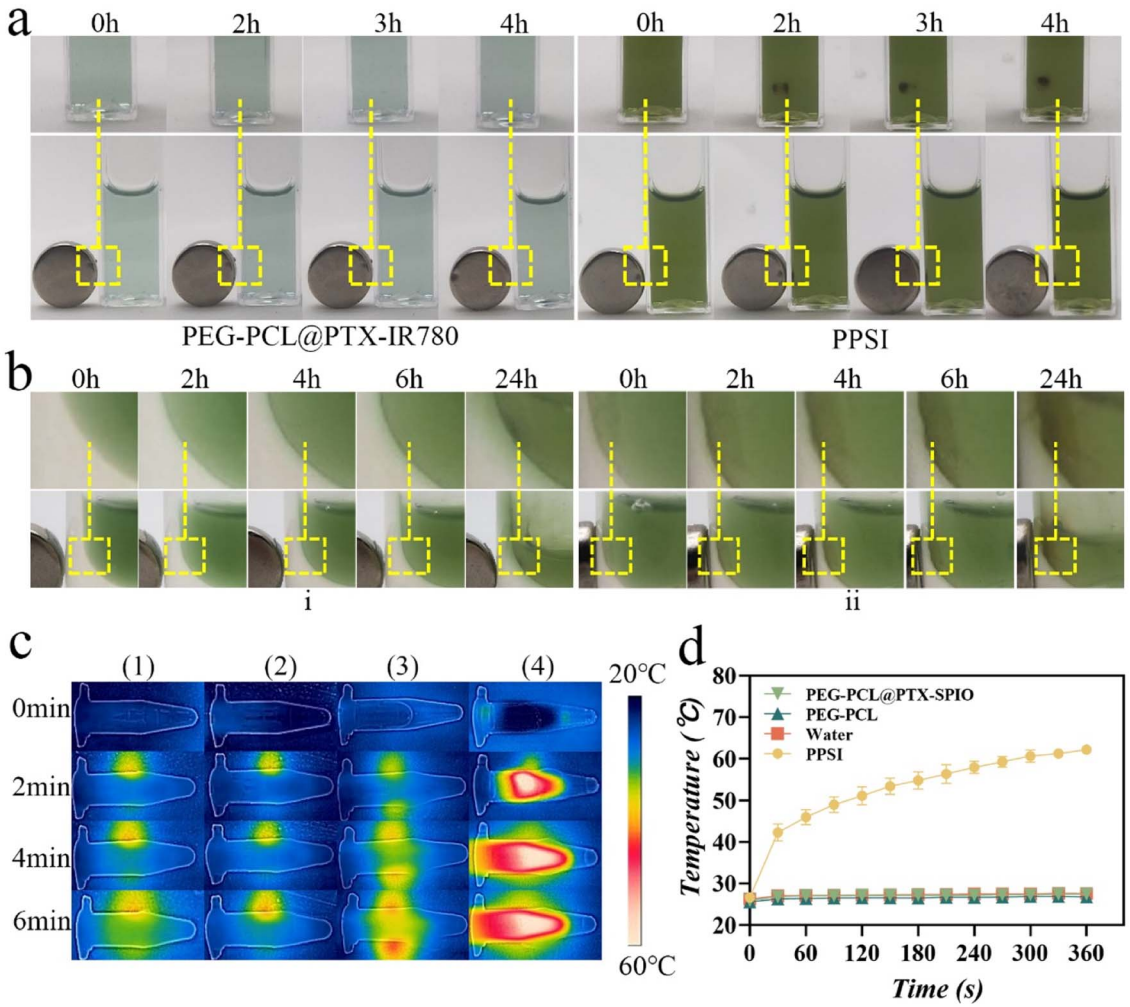

Fig. 3 Evaluation of magnetic responsiveness and photothermal effects of PPSI nanoparticles. (a) PPSI nanoparticles and PEG-PCL@PTX-IR780 nanoparticles under an external magnetic field in water for 4 h. (b) PPSI nanoparticles under an external magnetic field in agarose for 24 h: (i) side of neodymium magnet; (ii) front of neodymium magnet. (c) Temperatures of various groups imaged by using an infrared thermal imaging camera: (1) water; (2) PEG-PCL; (3) PEG-PCL@PTX-SPIO; (4) PPSI. (d) Temperatures of different groups under laser irradiation (808 nm, 2.0 W cm^{-2}, 6 min).

effect (PPSI + M) group compared to the other groups (Fig. 4a and b). This result confirmed that magnetic targeting facilitated the aggregation of more nanoparticles near the cells, thus improving the endocytosis of the drugs by the cells, which is a critical process for targeting PPSI nanoparticles in photothermal therapy.

In vitro cytotoxicity and therapeutic efficacy

An *in vitro* drug release study was implemented to confirm the drug release properties of nanoparticles. The simulated Ph environment revealed that the drug release rate was improved with decreasing pH. This phenomenon was attributed to the sensitivity of the nanoparticles, as the copolymers exhibited a series of behaviors, such as hydrolysis and degradation due to protonation under acidic conditions, resulting in a more rapid release in acidic media than in neutral media. Furthermore, the addition of the photosensitizer IR780 produced a photothermal effect that greatly promoted drug release (Fig. S2†). Laser irradiation possibly decreased the stability of the polymer shell, leading to the collapse of these nanoparticles, which may result in a slight increase in the PTX release rate. These findings demonstrated the ability of PPSI nanoparticles to respond to the tumor microenvironment and achieve proper drug action at the tumor site. Subsequently, we further evaluated the photothermal-chemotherapy cytotoxicity of the drug-loaded nanoparticles *in vitro*. The 4T1 cells were incubated with free drugs or PPSI nanoparticles followed by multiple interventions (with or without a laser or magnet).

As shown in Fig. 4c and d, there was no significant decrease in cell viability in the control group (PBS) and the irradiation-only group (PBS + L), indicating that a single laser did not have a noticeable killing effect on cells. Both free IR780 and PTX groups exhibited antitumor ability in tumor cells. A significant decrease in cell survival was observed in the PPSI + L (PEG-PCI@SPIO-PTX-IR780 with a laser) group compared to the

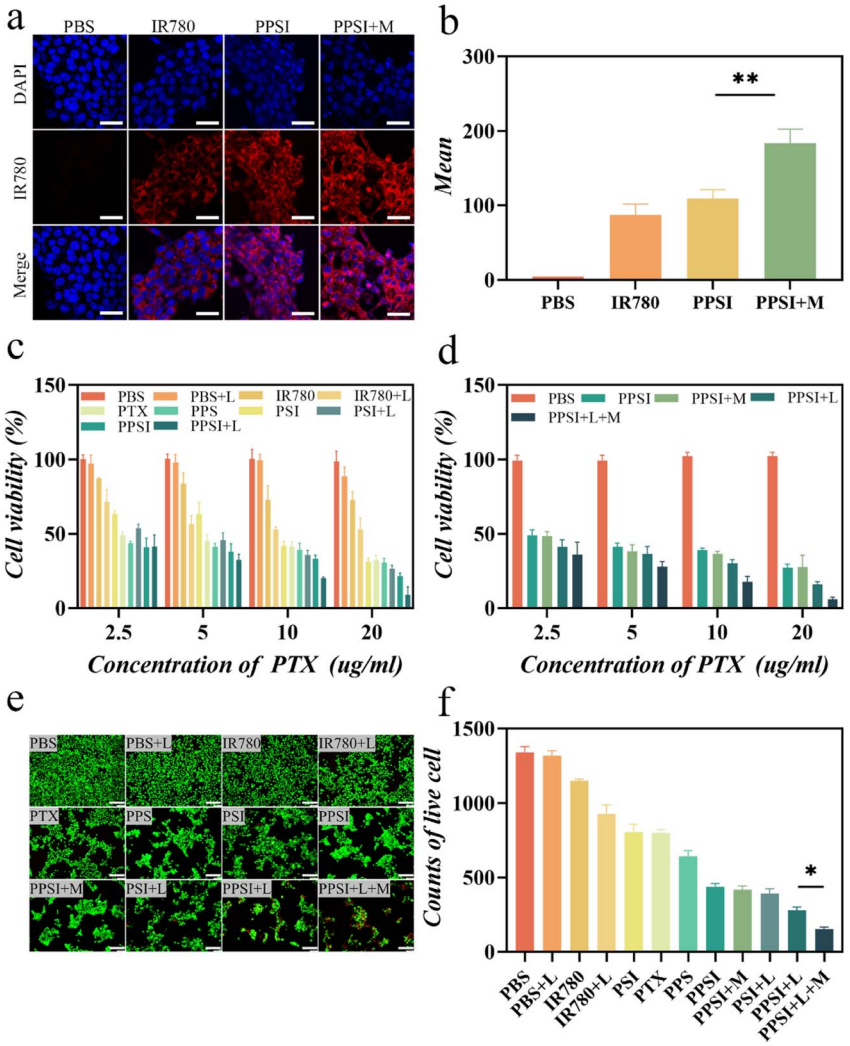

Fig. 4 Cell viability and uptake of PPSI nanoparticles. (a) and (b) Fluorescence images of 4T1 cells incubated with PPSI nanoparticles with or without magnetic iron at the bottom of the dish and fluorescence intensity analysis. (c) and (d) *In vitro* cytotoxicity and therapeutic efficacy of PPSI nanoparticles. (e) Calcein-AM/PI staining of groups with different experimental treatments. (f) Semi-quantitative analysis of live cells. Scale bars are 25 μm in (a) and 100 μm in (e). $P^* < 0.05$, $P^{**} < 0.001$.

IR780 ($p < 0.001$), IR780 + L (IR780 with a laser, $p < 0.001$), PSI (PEG-PCL@SPIO-IR780, $p < 0.001$), and PSI + L (PEG-PCL@SPIO-IR780 with a laser, $p < 0.05$) groups, suggesting that the efficacy of combined photothermal-chemotherapy is superior to that of single photothermal treatment. Compared with the PTX ($p < 0.001$) and PPS (PEG-PCL@SPIO-PTX, $p < 0.001$) groups, the cytostatic rate was significantly higher in the PPSI + L group, indicating that the efficacy of photothermal-chemotherapy combination therapy was superior to that of single chemotherapy. In addition, we intervened in the therapeutic efficacy of PPSI nanoparticles by applying external magnetic forces. Compared with the PPSI ($p < 0.001$), PPSI + L ($p < 0.05$), and PPSI + M (PEG-PCL@SPIO-PTX-IR780 with a magnet, $p < 0.001$) groups, the PPSI + L + M (PEG-PCL@SPIO-PTX-IR780 with a laser and magnet) group exhibited higher inhibition of tumor cell growth. This result suggested that locally applied external magnetic forces improved the anti-tumor effect of PPSI nanoparticles to some extent.

Moreover, the cytotoxicity of PPSI nanoparticles on cells was assessed by live/dead staining (Fig. 4e and f). Live-dead cell staining revealed that cells were viable in all groups, albeit in different proportions. Notably, the PPSI + L + M group showed potent tumor cell killing. These results, as well as the results of the *in vitro* cytotoxicity assay, indicated that PPSI nanoparticles possessed the efficacy of photothermal-chemotherapy and combined magnetic targeting action, which was preferable to single chemotherapeutic or photothermal treatments, and improved the inhibition of tumor growth, thus laying the foundation for subsequent studies.

Subsequently, the biocompatibility of the carrier was initially assessed before further experiments. Fibroblast 3T3 cells were incubated with different concentrations of PEG-PCL and PEG-PCL@SPIO nanoparticles for 24 h and 48 h to evaluate the toxicity of the carrier towards normal cells. The cell viability of 3T3 cells remained above 95% even with increasing concentrations of empty nanocarriers after 24 h and 48 h of incubation,

indicating excellent biocompatibility (Fig. S3†). These results suggested that PEG-PCL and PEG-PCL@SPIO had great potential as a carrier for biomedical applications.

In vivo distribution

To evaluate the accumulation of PPSI nanoparticles *in vivo*, we investigated the biodistribution of PPSI nanoparticles in a carcinoma in breast cancer models by inoculating 4T1 cells into the mammary fat pads of BALB/c mice. By integrating IR780, the nanoplatform could provide a dose-tracking ability. In a typical experiment, the fluorescence signal increased gradually and peaked at 48 h. Compared with the PPSI group, the PPSI + M group exhibited more drug accumulation (Fig. 5a and c). The *ex vivo* imaging revealed that the tumor aggregated more nanoparticles than other organs (Fig. 5b and d), indicating extraordinary tumor targeting of PPSI nanoparticles. In addition, the liver, the lung and the kidneys showed weak fluorescence.

It was observed that the stronger total fluorescence signal in the experimental group as well as the stronger signal in the liver after magnetic targeting may be attributed to the following factors. Firstly, free drugs modified by PEG-PCL can accumulate in tumor tissues through the EPR effect and reduced clearance by the endothelial reticular system,[34,35] while most of the free IR780 was easily and rapidly removed from blood circulation.[36] Secondly, PPSI may encounter obstacles when crossing the tumor vascular barrier only through the EPR effect. The intervention of external magnetism may prolong the drug's time at the tumor site to a certain extent. As a final point, the magnets in the PPSI + M group were briefly dislodged during fluorescence imaging, allowing some of the nanoparticles to re-enter blood circulation. On the one hand, the effect of an external magnetic field might prolong the nanoparticle time in blood circulation, and on the other hand, the nanoparticles might be agglomerated by the effect of the external magnetic field, resulting in an increase in the size of the nanoparticles, which are phagocytosed by the hepatic reticuloendothelial system and retained,[37,38] thus resulting in more fluorescent signals in the organs and tumor of the PPSI + M group.

Fluorescence imaging provides a visual window for tracking the drug delivery process in real time and understanding the extent of drug aggregation at the tumor site, thus providing a more appropriate therapeutic time point for subsequent combination treatment.[39,40] Thus, by imaging tumors fluorescently, the effect of drugs can be maximized and the effectiveness of combined photothermal-chemotherapy can be enhanced.

In Jang's study, it was shown that T_2-weighted MRI imaging capabilities existed in SPIO even at low doses, and that it was able to aggregate nanoparticles at the target site under magnetic guidance,[41] which is consistent with the results of *in vivo* imaging in small animals. The content of SPIO *in vivo* was

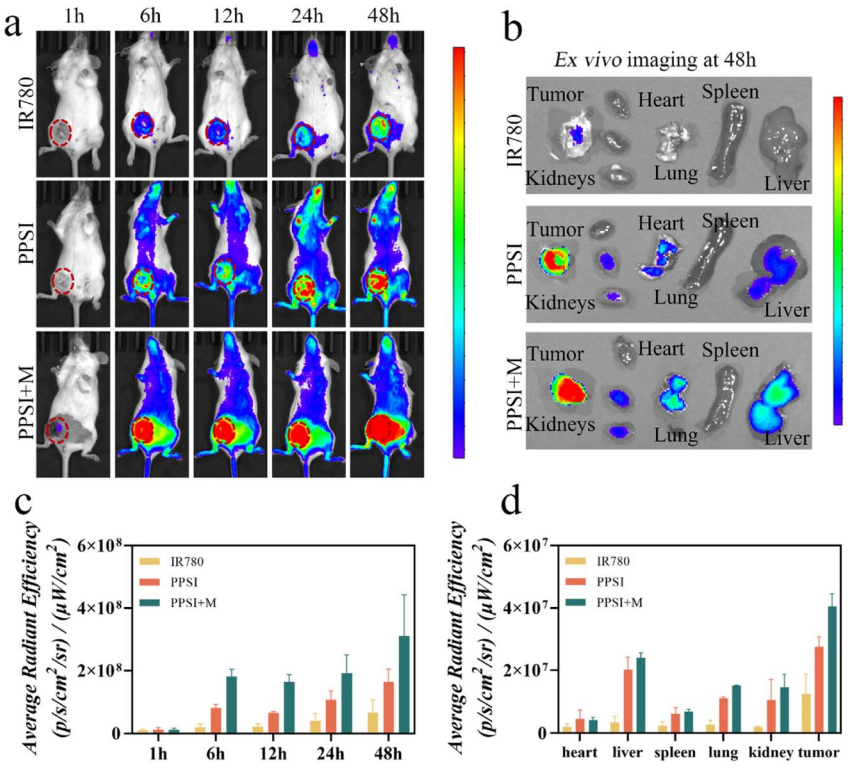

Fig. 5 The biodistribution of the nanoplatform was imaged *in vivo* and *ex vivo*. (a) Representative *in vivo* fluorescence images of the 4T1 tumor-bearing mice at different time points after intravenous injection of PPSI nanoparticles or free IR780. The red circle emphasizes the tumor region. (b) The *ex vivo* fluorescence images of major organs and tumors from mice 48 h after injection with the corresponding formulations. (c) Fluorescence intensity analysis of tumor sites in mice. (d) Fluorescence semi-quantitative analysis of the tumor and organs.

examined by ICP-MS, and Kang's study showed that the content of Fe at the tumor site was higher than that in the other untreated groups under magnetic guidance, and the extent of Fe accumulation at the tumor site was redundant compared to that in other organs,[42] which is consistent with the results of the fluorescence semi-quantitative analysis of the tumor site in the present study, suggesting that magnetic guidance could increase the accumulation of drugs in the tumor.

Overall, the PPSI nanoparticles demonstrated excellent tumor accumulation facilitated by magnetic navigation. The biodistribution of PPSI nanoparticles provided a solid foundation for further treatment.

Antitumor effect *in vivo*

PTX is a commonly utilized chemotherapeutic agent in clinical practice;[43] however, its limited distribution within tumors during practical application often results in suboptimal therapeutic outcomes.[44] Magnetically guided PPSI nanoparticles, to a certain extent, could increase the accumulation of drugs at the tumor site, thereby achieving an enhanced anti-tumor effect. Thus, to investigate the potential value of the nanoplatform, we further investigated the synergistic therapeutic effects of nanoparticles on 4T1 carcinoma mice models (Fig. 7a).

The successfully molded mice were randomly separated into 5 groups (saline, saline + L, IR780 + L, PPSI + L, and PPSI + L + M), to study the therapeutic differences between the combination treatment and single photothermal treatment, and separated into 6 groups (saline, PTX, PPSI, PPSI + L, PPSI + M, and PPSI + L + M) to study the therapeutic differences between combination therapy and single chemotherapy. The *in vivo* antineoplastic efficacy was assessed by recording the changes in tumor volume for 16 days.

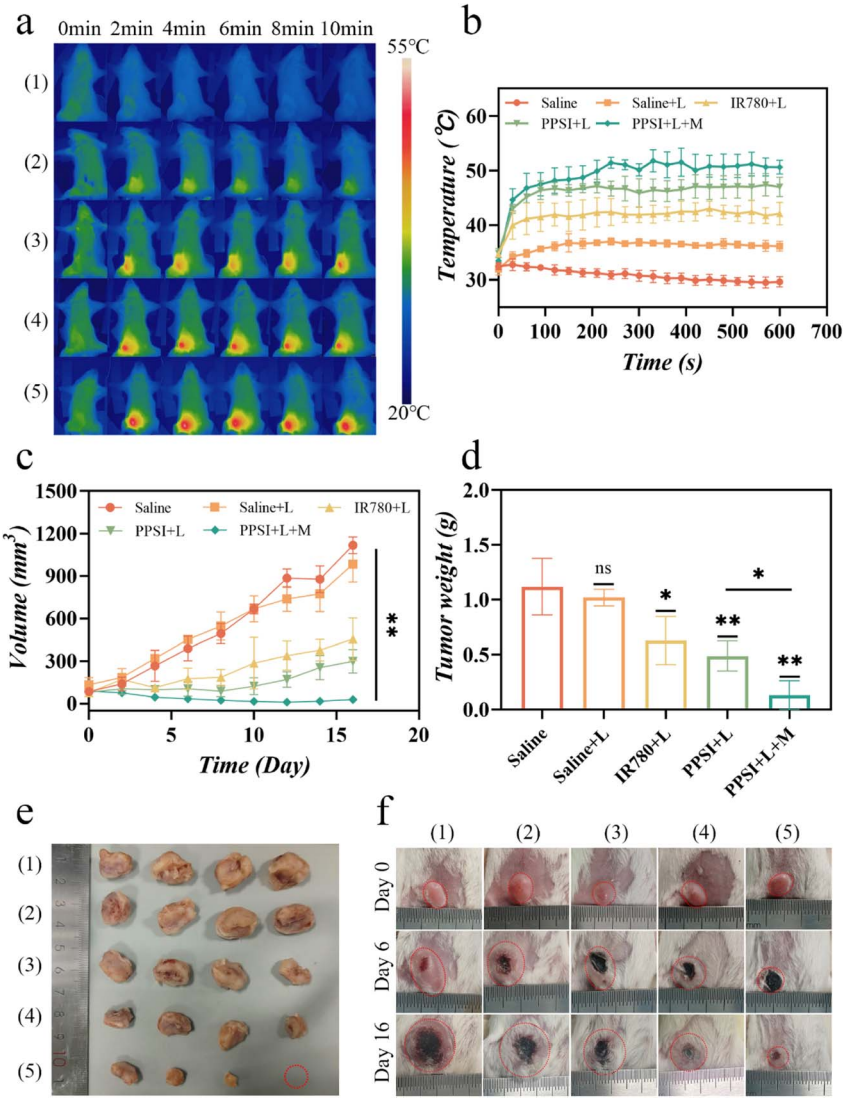

Fig. 6 Antitumor activity of PPSI nanoparticles. (a) *In vivo* photothermal warming image. (b) *In vivo* photothermal warming curve. (c) Tumor growth curves of mice treated with saline, saline + L, IR780 + L, PPSI + L, and PPSI + L + M. (d) Average tumor weight of each group on day 16. (e) Photographs of excised tumors from all groups on day 16. (f) Digital photos of tumors from all groups on day 0, 6, and 16 after treatment. The red circle emphasizes the tumor region. (1) Saline; (2) saline + L; (3) IR780 + L; (4) PPSI + L; (5) PPSI + L + M. $P^* < 0.05$ and $P^{**} < 0.001$.

The temperature of photothermal treatment with PPSI nanoparticles was examined in animals. During 10 min laser irradiation, the temperature at the local tumor of mice in the PPSI + L + M group reached a maximum of 55.1 °C, which was 5.4 °C and 10.3 °C higher than that of the PPSI + L group (49.7 °C) as well as the IR780 + L group (44.8 °C), respectively. In contrast, the maximum temperature in the saline + L group only rose to 37.9 °C during the 10 min irradiation period, failing to reach the minimum temperature for photothermal therapy.[45] These results indicated that PPSI nanoparticles possessed a good photothermal conversion effect, which provided a solid foundation for the subsequent inhibition of tumor growth (Fig. 6a and b).

As shown in Fig. 6c–f, treatment with the saline or saline + L group led to feeble tumor suppression efficacy, indicating that single laser irradiation could not have a therapeutic effect on the tumor. Compared with the IR780 + L group and PPSI + L group, the PPSI + L + M group had a better tumor inhibition effect. Observations on the body weights of the mice during treatment showed that the body weights of the mice in the treatment group did not fluctuate much, whereas the body weights of the saline group gradually decreased in the later stages of observation (Fig. S4a†). These results showed that the anti-tumor effect of photothermal-chemotherapy combined with magnetic targeting was more effective than that of single photothermal treatment and single photothermal-chemotherapy combination.

As shown in Fig. 7b, treatment with the PTX or PPSI group led to feeble tumor suppression efficacy in the absence of magnet or laser therapy. The PPSI + L + M group demonstrated the strongest inhibition of tumor growth compared to the other groups due to the magnetic attraction of nanoparticles. It facilitated more drug accumulation at the tumor site, leading to enhanced photothermal ablation and increased drug release triggered by the elevated temperature. Although mice in the PPSI + M group and PPSI + L + M group experienced decreased body weight at the beginning, they regained weight after the withdrawal of the drug at the end of the treatment cycle (Fig. S4b†). Experimental mice were euthanized on day 16, and their tumors were removed and analyzed (Fig. 7c–e). Tumor growth in the saline group was the fastest, while it was slightly inhibited in the PPSI or PTX groups. Additionally, the PPSI + L + M group exhibited significantly more effective suppression of tumor growth than the other treatment groups. These results indicated that synergistic photothermal-chemotherapy complemented by magnetic navigation had a superior impact on inhibiting tumor growth than that of single chemotherapy treatment and single photothermal-chemotherapy combination.

In addition, since the 4T1 tumor model is prone to breakage, manipulations, such as local hair removal and treatment after the mice were injected with tumor cells for modeling, will exacerbate their crusting, and thus the tumors of the experimental mice appeared black in Fig. 7e.

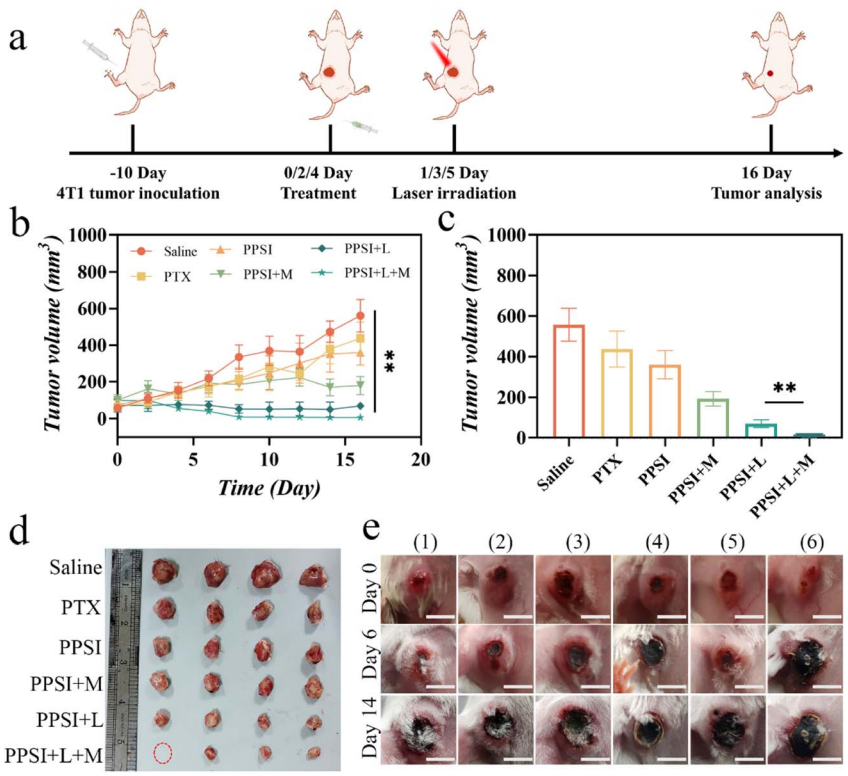

Fig. 7 Antitumor activity of PPSI nanoparticles. (a) Experimental design of animal research. (b) Tumor growth curves of mice treated with saline, PTX, PPSI, PPSI + M, PPSI + L, and PPSI + L + M. (c) Average tumor volume of each group on day 16. (d) Photographs of excised tumors from all groups on day 16. (e) Digital photos of tumors from all groups on day 0, 6, and 14 after treatment. (1) Saline; (2) PTX; (3) PPSI; (4) PPSI + M; (5) PPSI + L; (6) PPSI + L + M. $P^* < 0.05$ and $P^{**} < 0.001$.

To investigate the underlying mechanisms of tumor inhibition, pathological analysis was applied to tumors from treatment groups compared to single chemotherapy. The results of HE sections demonstrated that the areas of apoptosis and necrosis in the PPSI + L + M group were significantly more pronounced than in the other groups (Fig. 8a). Tumor slices stained with Ki-67 and TdT-mediated dUTP nick end labeling (TUNEL) (Fig. 8b and d and S5†) showed that the saline group exhibited vigorous tumor cell growth with a high proliferation rate and no significant cell apoptosis. The PTX, PPSI, and PPSI + M groups exhibited limited damage to tumor cells, while PPSI + L and PPSI + L + M groups exhibited extensive apoptosis in the tumor tissue. The Ki-67 positive cell/mm^2 exhibited a trend of saline > PTX > PPSI > PPSI + M > PPSI + L > PPSI + L + M, whereas the TUNEL positive cell per mm^2 exhibited a trend of PPSI + L + M > PPSI + L > PPSI + M > PPSI > PTX > saline, indicating that PPSI under a laser and magnetic targeting had the most potent tumor growth inhibitory effect. Additionally, cytokine levels (TNF-α) in tumor tissues were analyzed by immunohistochemistry (IHC) (Fig. 8c and S5†), and showed significantly higher values in PPSI + L + M and PPSI + L groups than in other groups. This finding suggested that photothermal therapy promoted proinflammatory factors, thereby enhancing the effectiveness of tumor therapy. These results suggested that nanoparticles can enhance the effectiveness of tumor therapy by promoting inflammation, inhibiting cell proliferation activity and directly killing tumor cells. Intriguingly, the HE sections of major organs of mice gathered on day 16 after drug injection displayed no significant pathological changes in any of the groups, compared to the saline group at the doses studied (Fig. S6†).

Hepatic and renal impairment were assessed by measuring four indices in the serum of the mice at the end of the observation period, namely AST, ALT, UREA, and CREA. The results showed that there was no significant difference between the treatment groups and the control group (Fig. S7a–d†).

The effect of nanoparticles on the blood system of the organism was assessed by performing hematological examinations on the blood of mice at the end of the observation period. The results showed that there were no significant differences in red blood cell level-related indices (HCT, RBC, and RDW), white blood cell level-related indices (WBC, NEUT, LYMPH, MONO, and BASO), platelet level-related indices (PLT and MPV), and hemoglobin-related indices (HGB and MCHC) between each treatment group and the control group (Fig. S7e–p†).

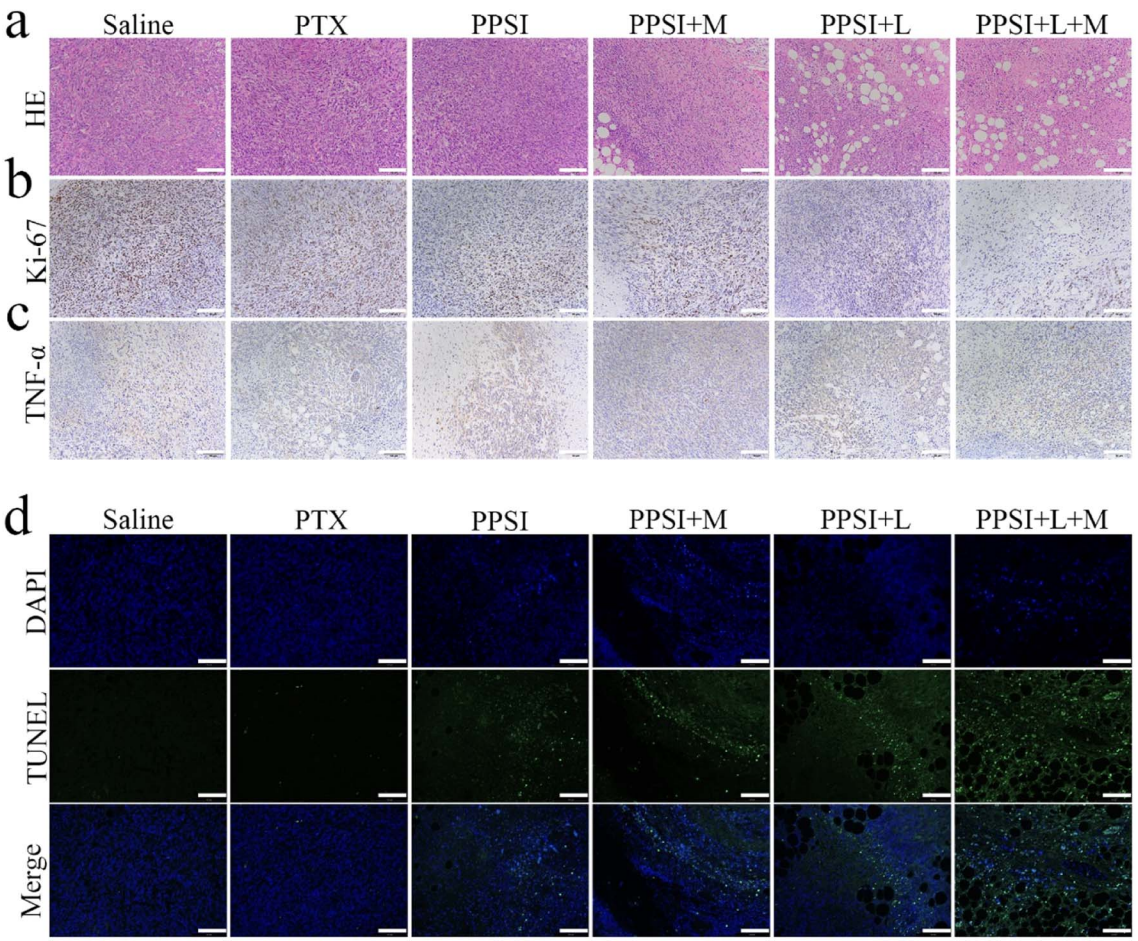

Fig. 8 Analysis of the underlying mechanism for the observed antitumor effect. (a–c) HE and IHC staining of Ki-67 and TNF-α in the six different treatment groups. (d) TUNEL staining in the groups with different interventions. The scale bars are 50 μm for HE, Ki-67 and TNF-α, and 100 μm for TUNEL.

Although PTX has been reported in the literature to have a myelosuppression effect in mice,[46,47] the leukocyte levels in the free PTX group as well as in the combined treatment groups in this experiment were not significantly different from those in the control group, although they were slightly lower.

In summary, our research has addressed the compatibility of the developed nanoparticles, ensuring their feasibility and reliability in clinical applications.

Conclusion

In this study, we developed a multifunctional polymeric nanoparticle for breast tumor imaging and therapy. The nanoparticles co-encapsulate PTX, SPIO, and IR780 to enable magnetically guided photothermal-chemotherapy combination therapy. The nanoparticles were passively targeted to 4T1 tumor cells by magnetic navigation. Under NIR laser irradiation, the encapsulated IR780 exhibited excellent photothermal conversion efficiency, leading to the effective release of PTX. The combination of PTX as a chemotherapeutic agent, SPIO as a magnetic navigational agent, and IR780 as a photothermal conversion agent enabled magnetically guided photothermal-chemotherapeutic combination therapy to further enhance the therapeutic effect. *In vitro* and *in vivo* experiments showed that the PPSI + L + M group had a superior therapeutic effect compared to the IR780 + L group, the PTX group and the PPSI + L group. These results demonstrated that the anti-tumor effect of magnetically guided photothermal-chemotherapy combination therapy was superior to that of single chemotherapy, single photothermal therapy and single photothermal-chemotherapy combination therapy. Furthermore, the developed nanoparticles exhibited positive *in vivo* biocompatibility, suggesting their high potential for clinical translation and application in the treatment of breast malignancies.

Data availability

The data that supported the findings of this study are available from the corresponding author upon reasonable request.

Conflicts of interest

The authors have declared that no competing interest exists.

Acknowledgements

This work was supported by the National Natural Science Foundation of China (81672380), Jiangsu Provincial Medical Innovation Center (CXZX202213), Drum Tower Hospital Youth Formation Program (2022-JCYJ-QP-59), Youth Fund of Jiangsu Province (BK20230142) and Nanjing Drum Tower Hospital Incubation Program. Y. P. F., H. M. Z., and J. H. Y. contributed equally to this work. Y. P. F., H. M. Z. and J. H. Y. performed the experiments; Y. X. Y. and C. R. C. analyzed the data; B. J. W., X. Y. and J. J. S. constructed mouse models *in vivo*; Y. P. F. and H. M. Z. wrote the paper; W. J. Z., C. Z. and Z. Y. commented on the study and revised the paper; W. J. Z. and C. Z. designed and supervised the research.

References

1 R. L. Siegel, K. D. Miller, H. E. Fuchs and A. Jemal, *Ca-Cancer J. Clin.*, 2022, **72**, 7–33.
2 K. D. Miller, L. Nogueira, T. Devasia, A. B. Mariotto, K. R. Yabroff, A. Jemal, J. Kramer and R. L. Siegel, *Ca-Cancer J. Clin.*, 2022, **72**, 409–436.
3 M. R. Dethe, A. Prabakaran, H. Ahmed, M. Agrawal, U. Roy and A. Alexander, *J. Controlled Release*, 2022, **343**, 217–236.
4 H. J. Burstein, G. Curigliano, S. Loibl, P. Dubsky, M. Gnant, P. Poortmans, M. Colleoni, C. Denkert, M. Piccart-Gebhart, M. Regan, H. J. Senn, E. P. Winer and B. Thurlimann, *Ann. Oncol.*, 2019, **30**, 1541–1557.
5 A. G. Waks and E. P. Winer, *JAMA, J. Am. Med. Assoc.*, 2019, **321**, 288–300.
6 K. J. Ruddy and P. A. Ganz, *Jama*, 2019, **321**, 1716–1717.
7 R. H. Fang, W. Gao and L. Zhang, *Nat. Rev. Clin. Oncol.*, 2023, **20**, 33–48.
8 L. Zhong, Y. Li, L. Xiong, W. Wang, M. Wu, T. Yuan, W. Yang, C. Tian, Z. Miao, T. Wang and S. Yang, *Signal Transduction Targeted Ther.*, 2021, **6**, 201.
9 A. G. Arranja, V. Pathak, T. Lammers and Y. Shi, *Pharmacol. Res.*, 2017, **115**, 87–95.
10 S. Roy, N. Bag, S. Bardhan, I. Hasan and B. Guo, *Adv. Drug Delivery Rev.*, 2023, **197**, 114821.
11 S. Guo, D. Gu, Y. Yang, J. Tian and X. Chen, *J. Nanobiotechnol.*, 2023, **21**, 348.
12 P. Boix-Montesinos, P. M. Soriano-Teruel, A. Armiñán, M. Orzáez and M. J. Vicent, *Adv. Drug Delivery Rev.*, 2021, **173**, 306–330.
13 J. J. Liu, Z. Wang, L. M. Nie, Y. Y. Zhu, G. Li, L. L. Lin, M. Chen and G. J. Zhang, *Eur. J. Nucl. Med. Mol. Imaging*, 2022, **49**, 847–860.
14 M. Afzal, A. Ameeduzzafar, K. S. Alharbi, N. K. Alruwaili, F. A. Al-Abassi, A. A. L. Al-Malki, I. Kazmi, V. Kumar, M. A. Kamal, M. S. Nadeem, M. Aslam and F. Anwar, *Semin. Cancer Biol.*, 2021, **69**, 279–292.
15 Z. Ma, N. Li, B. Zhang, Y. Hui, Y. Zhang, P. Lu, J. Pi and Z. Liu, *J. Nanobiotechnol.*, 2020, **18**, 123.
16 Z. Liu, J. Li, W. Chen, L. Liu and F. Yu, *Biomaterials*, 2020, **232**, 119685.
17 E. S. McDonald, A. S. Clark, J. Tchou, P. Zhang and G. M. Freedman, *J. Nucl. Med.*, 2016, **57**(Suppl 1), 9s–16s.
18 Y. Zhong, T. Li, Y. Zhu, J. Zhou, T. O. Akinade, J. Lee, F. Liu, D. Bhansali, Y. H. Lao, C. H. Quek, D. Shao and K. W. Leong, *ACS Nano*, 2022, **16**, 20430–20444.
19 R. Q. Yang, P. Y. Wang, K. L. Lou, Y. Y. Dang, H. N. Tian, Y. Li, Y. Y. Gao, W. H. Huang, Y. Q. Zhang, X. L. Liu and G. J. Zhang, *Adv. Sci.*, 2022, **9**, e2104728.
20 Y. Wang, L. Jiang, Y. Zhang, Y. Lu, J. Li, H. Wang, D. Yao and D. Wang, *ACS Appl. Mater. Interfaces*, 2020, **12**, 33564–33574.
21 Y. Xing, T. Ding, Z. Wang, L. Wang, H. Guan, J. Tang, D. Mo and J. Zhang, *ACS Appl. Mater. Interfaces*, 2019, **11**, 13945–13953.

22 X. Liu, C. Wang, H. Ma, F. Yu, F. Hu and H. Yuan, *Adv. Healthcare Mater.*, 2019, **8**, e1801486.
23 Z. Yang, R. Cheng, C. Zhao, N. Sun, H. Luo, Y. Chen, Z. Liu, X. Li, J. Liu and Z. Tian, *Theranostics*, 2018, **8**, 4097–4115.
24 Y. Guo, X.-Y. Wang, Y.-L. Chen, F.-Q. Liu, M.-X. Tan, M. Ao, J.-H. Yu, H.-t. Ran and Z.-X. Wang, *Acta Biomater.*, 2018, **80**, 308–326.
25 F. Benyettou, M. Alhashimi, M. O'Connor, R. Pasricha, J. Brandel, H. Traboulsi, J. Mazher, J. C. Olsen and A. Trabolsi, *ACS Appl. Mater. Interfaces*, 2017, **9**, 40006–40016.
26 N. Sharma, K. Bietar and U. Stochaj, *Biochim. Biophys. Acta, Rev. Cancer*, 2022, **1877**, 188703.
27 E. Pavitra, B. Dariya, G. Srivani, S. M. Kang, A. Alam, P. R. Sudhir, M. A. Kamal, G. S. R. Raju, Y. K. Han, B. Lakkakula, G. P. Nagaraju and Y. S. Huh, *Semin. Cancer Biol.*, 2021, **69**, 293–306.
28 D. Gao, B. Zhang, Y. Liu, D. Hu, Z. Sheng, X. Zhang and Z. Yuan, *Theranostics*, 2019, **9**, 5315–5331.
29 I. Roy, S. Krishnan, A. V. Kabashin, I. N. Zavestovskaya and P. N. Prasad, *ACS Nano*, 2022, **16**, 5036–5061.
30 S. Li, S. Xu, X. Liang, Y. Xue, J. Mei, Y. Ma, Y. Liu and Y. Liu, *Adv. Healthcare Mater.*, 2021, **10**, e2100078.
31 P. Grossen, D. Witzigmann, S. Sieber and J. Huwyler, *J. Controlled Release*, 2017, **260**, 46–60.
32 X. Li, L. Hetjens, N. Wolter, H. Li, X. Shi and A. Pich, *J. Adv. Res.*, 2023, **43**, 87–96.
33 H. Zhu, D. Qin, Y. Wu, B. Jing, J. Liu, D. Hazlewood, H. Zhang, Y. Feng, X. Yang, M. Wan and D. Wu, *ACS Appl. Mater. Interfaces*, 2018, **10**, 29251–29259.
34 X. Li, Y. Gao, H. Li, J.-P. Majoral, X. Shi and A. Pich, *Prog. Mater. Sci.*, 2023, **140**, 101170.
35 M. Gong, Y. Huang, H. Feng, J. Lin, A. Huang, J. Hu, Q. Tang, X. Zhu, S. Han, J. Lu and J. Wang, *J. Controlled Release*, 2023, **355**, 68–84.
36 Y. Yin, L. Gao, P. Sun, L. Zeng, Q. Zhao, S. Chen, J. Liu and L. Wang, *Acta Biomater.*, 2023, **172**, 395–406.
37 Y. Lu, Q. Luo, X. Jia, J. P. Tam, H. Yang, Y. Shen and X. Li, *J. Pharm. Anal.*, 2023, **13**, 239–254.
38 J. Wang, P. Chen, Y. Dong, H. Xie, Y. Wang, F. Soto, P. Ma, X. Feng, W. Du and B. F. Liu, *Biomaterials*, 2021, **276**, 121056.
39 G. Yang, M. Li, T. Song, X. Chen, H. Zhang, X. Wei, N. Li, T. Li, X. Qin, S. Li, F. You, C. Wu, W. Zhang, Y. Liu and H. Yang, *Adv. Healthcare Mater.*, 2022, **11**, e2201615.
40 W. Li, H. Xin, Y. Zhang, C. Feng, Q. Li, D. Kong, Z. Sun, Z. Xu, J. Xiao, G. Tian, G. Zhang and L. Liu, *Small*, 2022, **18**, e2205647.
41 S. B. Jang, S. M. Jin, H. S. Kim, Y. Y. Jeong, S. J. Lee, S. Hahn, H. Lee, H. S. Lee, J. H. Kim and D. Y. Lee, *Biomaterials*, 2022, **287**, 121679.
42 K. Ma, S. Xu, T. Tao, J. Qian, Q. Cui, S. U. Rehman, X. Zhu, R. Chen, H. Zhao, C. Wang, Z. Qi, H. Dai, X. Zhang, C. Xie, Y. Lu, H. Wang and J. Wang, *Proc. Natl. Acad. Sci. U. S. A.*, 2022, **119**, e2211228119.
43 X. Wang, L. Ye, W. He, C. Teng, S. Sun, H. Lu, S. Li, L. Lv, X. Cao, H. Yin, W. Lv and H. Xin, *J. Controlled Release*, 2022, **345**, 786–797.
44 A. S. Widjaya, Y. Liu, Y. Yang, W. Yin, J. Liang and Y. Jiang, *J. Controlled Release*, 2022, **344**, 62–79.
45 M. Overchuk, R. A. Weersink, B. C. Wilson and G. Zheng, *ACS Nano*, 2023, **17**, 7979–8003.
46 R. Kinoshita, Y. Ishima, V. T. G. Chuang, H. Nakamura, J. Fang, H. Watanabe, T. Shimizu, K. Okuhira, T. Ishida, H. Maeda, M. Otagiri and T. Maruyama, *Biomaterials*, 2017, **140**, 162–169.
47 V. Demečková, P. Solár, G. Hrčková, D. Mudroňová, B. Bojková, M. Kassayová and S. Gancarčiková, *Biomed. Pharmacother.*, 2017, **89**, 245–256.